J Math Chem (2013) 51:2608–2637
DOI 10.1007/s10910-013-0244-6

ORIGINAL PAPER

Resolution enhancement as a key step towards clinical implementation of Padé-optimized magnetic resonance spectroscopy for diagnostic oncology

Dževad Belkić · Karen Belkić

Received: 24 June 2013 / Accepted: 27 July 2013 / Published online: 15 August 2013

Abstract Our overall aim is for the full potential of magnetic resonance spectroscopy (MRS) and magnetic resonance spectroscopic imaging (MRSI) to be realized in oncology. This requires mathematics, without which encoded MRS data are entirely uninterpretable. Mathematics based on the conventional approach, the fast Fourier transform (FFT), and ambiguous fittings of Fourier spectra cannot fulfill the rigorous demands of oncology. It is vital to go beyond the FFT and fitting, to obtain reliable quantitative information via MRS about the metabolic content of tissue. None of the available MRS fitting algorithms could provide the clinically needed information with certainty, namely, the metabolite concentrations. Our more advanced method, the fast Padé transform (FPT) is firmly established as a stable, high-resolution processor, with which metabolite concentrations are unequivocally generated for in vitro MRS data associated with prostate, breast and ovarian cancer. Validation of the FPT has also been performed for in vivo MRS of normal human brain from clinical magnetic resonance scanners (1.5 T) as well as from 4 to 7 T scanners. The FPT successfully handles major problems hindering more widespread clinical application of MRS and MRSI, such as separation of noise from signal, resolution of very dense spectra with multiplet resonances (prostate) and overlapping metabolite resonances (breast, brain). In the present paper, we focus upon the implications of resolution enhancement by the FPT. We conclude that the manner by which the FPT achieves its high resolution accuracy dictates

Dž. Belkić (✉) · K. Belkić
Department of Oncology and Pathology, Karolinska Institute, P.O. Box 260, 171 76 Stockholm, Sweden
e-mail: Dzevad.Belkic@ki.se

K. Belkić
School of Community and Global Health, Claremont Graduate University, Claremont, CA, USA

K. Belkić
Institute for Prevention Research, University of Southern California School of Medicine,
Los Angeles, CA, USA

a major reformulation of the concept of data acquisition by encoding a small number of short transient time signals to secure good signal-noise ratio. Padé-guided MRS has distinct clinical advantages in combining improved diagnostic accuracy of MRS with shorter examination times. This shortens turn-around time for patients, making MRS efficient and cost-effective. With Padé-based quantification plus FPT-guided encoding of MRS and MRSI data, MRS can become a reliable, cost-effective tool for diagnostics and various aspects of patient care within oncology.

Keywords Magnetic resonance spectroscopy · Quantification · Mathematical optimization · Padé approximant · Resolution enhancement · Radiation therapy · Encoding strategy

Abbreviations

PA	Padé approximant
FPT	Fast Padé transform
DFF	Denoising Froissart filter
PLQ	Padé-linear quadratic model
FFT	Fast Fourier transform
MR	Magnetic resonance
MRI	Magnetic resonance imaging
MRS	Magnetic resonance spectroscopy
MRSI	Magnetic resonance spectroscopic imaging
NMR	Nuclear magnetic resonance
FID	Free induction decay
MB	Megabyte
SNR	Signal-noise ratio
SNS	Signal-noise separation
RT	Radiation therapy
BPH	Benign prostatic hypertrophy
PSA	Prostate specific antigen
ppm	Parts per million
RMS	Root mean square
ww	Wet weight
Iso	Isoleucine
Val	Valine
Thr	Threonine
Lac	Lactate
Ala	Alanine
Lys	Lysine
Met	Methionine
Gln	Glutamine
Cr	Creatine
Crn	Creatinine
Cho	Choline

tCho	Total choline
Glc	Glucose
GPC	Glycerophosphocholine
PC	Phosphocholine
PE	Phosphoethanolamine

1 Introduction

In order for the full potential of magnetic resonance spectroscopy (MRS) and magnetic resonance spectroscopic imaging (MRSI) to be realized in oncology, mathematics are required. Without mathematics, the encoded MRS data are entirely uninterpretable. Mathematics based on the conventional fast Fourier transform (FFT), and ambiguous fittings of Fourier spectra cannot fulfill the rigorous demands of oncology. It is essential to offer a different vision from the FFT and fitting in order to obtain reliable quantitative information via MRS about the metabolic content of tissue. None of the existing MRS fitting algorithms is capable of providing the clinically needed information with certainty, especially the metabolite concentrations. Our more advanced method, the fast Padé transform (FPT) is firmly established as a stable, high-resolution processor [1–6], with which metabolite concentrations are unequivocally reconstructed from in vitro MRS data associated with prostate, breast and ovarian cancer [4,6–11]. Validation of the FPT has also been performed for in vivo MRS of normal human brain from clinical MR scanners (1.5 T) as well as from 4 to 7 T scanners [1,2,4,12–14]. Thus, the FPT can successfully handle major problems hindering more widespread clinical application of MRS such as separation of noise from signal [4,5,11,15], resolution of very dense spectra with multiplet resonances (prostate) [4,7,14] and overlapping metabolite resonances (breast, brain) [1–4,8,9,13].

Magnetic resonance is one of the leading diagnostic modalities within oncology. Magnetic resonance imaging (MRI) is highly sensitive for detecting cancer, but often insufficiently specific to distinguish malignant from non-cancerous pathology. Specificity can be improved by MRS which detects the metabolic features of cancer. Leading experts consider MRS to have the potential to revolutionize cancer diagnostics, image-guided surgery and target definition for radiation therapy (RT) [16–23]. More robust signal processing within MRS is crucial for achieving this potential, as emphasized by the U.S. National Cancer Institute [16]. It is here that the fast Padé transform can make a unique contribution.

One might wonder why would progress in MRS for oncology depend so critically upon mathematical optimization? This is the case because mathematical methods are needed since the measured MR data (time signals) cannot be interpreted directly. These MR time signals must be mapped via mathematics into the frequency domain to visualize the spectrum with peaks characterizing the tissue metabolites. The positions, widths, heights and phases are the spectral parameters of these peaks that determine the metabolite resonant frequencies, relaxation times and concentrations. Spectral analysis is an inverse problem where the measured result (time signal) is known, but its constituents (the spectral parameters) are unknown. Inverse problems are very common in medicine, indeed, through the familiar concept “the outcome is known but

the cause(s) are to be found" [1,4]. A major drawback of the FFT is that, as a single frequency-dependent polynomial F_N for N signal points, only the total shape spectrum (envelope) through non-parametric estimation can be obtained. The FFT cannot solve the quantification problem, which is the main task of MRS. To extract metabolite concentrations from an FFT spectrum comprised of metabolite peaks, fitting is used in post-processing by guessing the number of components underlying each peak. This inevitably generates false peaks (over-fitting or over-modeling) or fails to identify true resonances (under-fitting or under-modeling). Either case introduces new dilemmas to MRS and these are anathema to clinicians.

The FPT overcomes these defects via better-equipped mathematics as the ratio of two frequency-dependent polynomials P_K/Q_K ($2K \leq N$) that are extracted uniquely and directly from the investigated time signal. The total shape spectrum in the FPT is obtained at any desired frequency, and not just at the pre-assigned Fourier grid from the FFT. This gives the Padé-brought *interpolation* capability. Unlike the FFT, the FPT is also a reliable *extrapolator* [1–4]. These two features provide high resolution performance of the FPT. The FPT can work as a parametric estimator by solving the quantification problem via reconstruction of the exact number K of metabolites and their $2K$ genuine parameters (complex frequencies and complex amplitudes). In quantification by the FPT, the total number of resonances (K) is not surmised, but is treated as another spectral parameter to be reconstructed. This is achieved through signal-noise separation (SNS) [2,3,15] by which a genuine signal is distinguished from noise. The spectral parameters permit obtaining the component shape spectra for each metabolite. The total shape spectrum is the sum of K metabolite spectra. Robust error analysis is performed by searching for constancy of the retrieved spectral parameters and the resulting stability of the component and total shape spectra. Self-contained cross-checking and validation are provided by two different variants of the FPT, denoted by $\text{FPT}^{(+)}$ and $\text{FPT}^{(-)}$, that are initially defined inside and outside the unit circle, respectively, in the complex frequency plane [1–4]. When convergence is achieved by these two variants to the same reconstructed spectral parameters for all physical resonances, exact quantification of the examined time signal is verified to be complete. The FPT is the method of choice for MRS, since the diagnostically relevant concentrations of genuine metabolites are extracted uniquely and accurately from the reconstructed spectral parameters. Thereby, the FPT-generated metabolite concentrations become the long-sought gold-standard for diagnostics via MRS.

2 Cancer diagnostics through magnetic resonance: highlights for four key problem areas

2.1 Brain tumors

Within neuro-oncology, the potential of MRS/MRSI is well appreciated, as reviewed in Refs. [4,14,18,20,24,25]. Since the most delicate clinical decisions are made, maximally reliable information is sought. In no other area of oncology are MRS/MRSI so widely incorporated into clinical practice, as one of the key modalities for brain tumor diagnostics and management. The limitations of the FFT are all the more striking. Thus,

e.g., rather than obtaining accurate concentrations for some 25 metabolites, as can readily be achieved by the FPT [2,3,13,26], with the FFT much of neuro-diagnostics through MRS has been reduced to a semi-quantitative approach, based upon metabolite ratios, most often choline to creatine. Within radiation neuro-oncology, our recent study [26] shows that many recurrent primary brain tumors are thereby misclassified as radiation necrosis. Thus, the need to apply the FPT to post-RT data was underscored, since it provides much richer and more reliable metabolic information that would better distinguish brain tumor recurrence from post-RT necrosis [26].

2.2 Prostate cancer

Compared to MRI, in vivo MRSI can help: (a) differentiate between prostate cancer and benign prostatic hypertrophy (BPH), (b) find optimal site(s) for biopsy, (c) detect extracapsular extension, (d) select treatment modality as well as timing and (e) assess tumor regression versus recurrence after treatment [4,14,19,20,27]. Within RT, in vivo MRSI has been used to help detect the dominant intra-prostatic lesion that should receive a boost dose [14]. The ratio of two MR-observable metabolites, choline at ∼3.2 parts per million (ppm) and citrate (∼2.5–2.7 ppm) has been the cornerstone of prostate cancer diagnostics. Citrate is an indicator of healthy secretory activity of prostate epithelia, while choline reflects phospholipid metabolism of cell membranes, and is a marker of cell proliferation. There are however important exceptions: with metabolic atrophy due to radiation or hormonal therapy or in stromal prostate tissue, citrate levels are low without cancer being present. With BPH, citrate can be high despite coexistent malignancy. In our textbook [28], citrate and choline alone were noted to be insufficiently accurate to distinguish various patterns of prostatic disease. Moreover, MRS for prostate cancer has been insufficiently sensitive for analyzing smaller lesions. While showing some promise for distinguishing high- versus low-risk prostate cancer, FFT-processed MRS does not provide unequivocal results [29]. Limitations in resolution and interpretation of data from MRS are challenges in prostate cancer diagnostics, staging and surveillance [30]. In vitro MRS applied to extracted prostate specimens gives more insight into the metabolic activity of cancerous prostate tissue [31]. Still, the multiplets and closely-overlapping resonances of different metabolites in prostate spectra pose problems for quantification that are not solved by the FFT and follow-up fitting [31]. The fast Padé transform has been applied to MRS data as encoded in vitro from normal glandular and stromal prostate and prostate cancer [31]. The FPT retrieved the genuine biochemical content of the scanned tissue for these three cases using only a fraction of the full signal length. The Padé absorption component spectra resolved all physical resonances, including multiplet resonances and overlapping peaks of different metabolites. Thus, the FPT yielded the unique metabolite concentrations for distinguishing normal from cancerous prostate tissue [4,7,14].

2.3 Breast cancer

Although contrast-enhanced MRI is generally very sensitive, false negatives do occur for small breast cancers, especially those that do not selectively take up contrast.

However, the main drawback of MRI is lack of specificity (false positives) [32]. Specificity is improved via in vivo MRS, as per data published for more than 200 breast lesions [4,33,34]. In these studies, the FFT and fitting were used, with consequent limitations in resolution, signal-noise ratio (SNR), and restricted estimates of only one composite compound, which is total choline (tCho). Especially problematic is the limited possibility of MRS to distinguish smaller tumors (< 2 cm) from benign lesions [35]. Specificity is reduced with exclusive reliance upon tCho since increased total choline can be seen in benign breast pathology and during lactation. Total choline is often undetected in small tumors that are misclassified as benign [36]. The high resolution of in vitro MRS gives more insight into metabolic activity of cancerous breast. We performed extensive multivariate analysis [37] of such data from extracted breast specimens [38] revealing rich spectroscopic information in closely-overlapping resonances for detecting breast cancer. The FPT has been applied to MRS data as encoded in vitro from (i) normal, non-infiltrated breast tissue (ii) benign pathology (fibroadenoma) and (iii) malignant breast tissue [38] with exact reconstruction of the tissues' genuine biochemical content from the input time signals [8,9,13]. The Padé absorption spectra resolved all the extracted physical metabolites, even those that were completely overlapping (phosphocholine (PC) and phosphoethanolamine (PE) at 3.22 ppm). The FPT precisely quantified the physical resonances as encountered in normal versus benign versus malignant breast, including diagnostically important metabolites, such as lactate, choline and PC versus glycerophosphocholine (GPC) that very closely overlap. Specifically, PC is a marker of breast cancer. The PC/GPC ratios were computed as 0.59, 1.57 and 2.6, respectively demonstrating the so-called "GPC to PC switch", associated with malignant transformation [22].

2.4 Ovarian cancer

Standard diagnostic methods are generally inadequate for early detection of ovarian cancer. Due to the small size and motion of the ovary, in vivo MRS has limited resolution and poor SNR [4,28,39]. Yet, a rich store of MRS-observable compounds distinguishes benign from cancerous ovarian lesions when in vitro MRS is applied with its attendant high resolution. Concentrations of very closely-lying resonances e.g. isoleucine (Iso) and valine (Val) at approximately 1.02 ppm and 1.04 ppm differ significantly in these two types of lesions. The high concentrations of these amino-acids are protein breakdown products due to necrosis and proteolysis. Generally, MRS has been viewed as the potential method of choice for detecting early stage ovarian cancer, insofar as the current obstacles hindering acquisition of high quality time signals and their subsequent quantitative analysis and interpretation are surmounted [40]. In applications [4,10,11,13] of the FPT to time signals associated with MRS data for benign and cancerous ovarian cyst fluid from Ref. [40], all the spectral parameters of every physical metabolite were exactly reconstructed by using very small fractions of the full time signals [4,10,11]. By contrast, with the FFT, the spectra generated at these short signal lengths were totally uninterpretable [4,10,13]. Resorting to long signal lengths worsens SNR in the FFT, since at longer acquisition times noise becomes detrimental for any Fourier-based attempts to improve resolution. When the FFT and

fitting are used, the so-named "spectral crowding" becomes a major problem in splitting apart the closely-lying resonances. Our results [4,10,11,13] demonstrate that the FPT can separate noise from signal and thus improve SNR and resolution, which have been a major barrier to in vivo applications of MRS for ovarian cancer diagnostics.

Overall, in conclusion to this section, the achievements to date of the fast Padé transform in MRS-based cancer diagnostics [1–15], motivate the need for direct clinical implementation of the FPT within oncology. The present paper provides critical new steps for that process, in relation to resolution enhancement and the practical implications thereof.

3 The fast Padé transform

3.1 The structured time signal

The typical MRS time signal $\{c_n\}$, or free induction decay (FID) curve is given by the following linear combination of K complex exponentially attenuated harmonics:

$$c_n = \sum_{k=1}^{K} d_k \mathrm{e}^{in\tau\omega_k}, \qquad 0 \le n \le N-1\,, \tag{1}$$

where N is the total signal length and τ is the sampling time. Quantities $\{\omega_k\}$ and $\{d_k\}$ are the fundamental complex frequencies and complex amplitudes, respectively. This signal has a structure which is described though the set of the fundamental frequencies and the corresponding amplitudes $\{\omega_k, d_k\}$ $(1 \le k \le K)$ of the system which produced the FID after being exposed to an excitation. The particular form (1) is prescribed by the quantum-mechanical description of general time evolution of any dissipative system which is set in an oscillatory motion by external perturbations. The system operator $\hat{\Omega}$ for any dissipative dynamics is a non-Hermitean operator which, therefore, has a spectrum built from complex eigenvalues $\{\omega_k\}$. This maps the complex exponential from (1) into the form:

$$\begin{aligned} \mathrm{e}^{i\omega_k n\tau} &= \mathrm{e}^{in\tau\mathrm{Re}(\omega_k)-n\tau\mathrm{Im}(\omega_k)} \\ &= \mathrm{e}^{-n\tau\mathrm{Im}(\omega_k)}\{\cos(n\tau\mathrm{Re}(\omega_k)) + i\sin(n\tau\mathrm{Re}(\omega_k))\}, \quad \mathrm{Im}(\omega_k) > 0. \end{aligned} \tag{2}$$

We see from here that dissipative systems, i.e. the systems that lose energy during their forced motions, must necessarily exhibit exponential damping via $\mathrm{e}^{-n\tau\mathrm{Im}(\omega_k)}$ of forced oscillations whose non-attenuated part is described by the purely trigonometric function $\cos(n\tau\mathrm{Re}(\omega_k)) + i\sin(n\tau\mathrm{Re}(\omega_k)) = \mathrm{e}^{in\tau\mathrm{Re}(\omega_k)}$ of constant (unity) amplitude.

3.2 The exact finite-rank Green function or response function

The exact spectrum is defined by the finite-rank Green function at any frequency ω in terms of the time signal points $\{c_n\}$ from (1) as follows:

$$G_N(z^{-1}) = \frac{1}{N}\sum_{n=0}^{N-1} c_n z^{-n}, \qquad z^{-1} = \mathrm{e}^{-in\tau\omega}. \tag{3}$$

Inserting c_n from (1) into (3) permits the exact summation over n by means of the binomial formula $\sum_{n=0}^{N-1} u^n = (1-u^N)/(1-u)$ with the result:

$$G_N(z^{-1}) = \frac{1}{N}\sum_{k=1}^{K} d_k \frac{1-(z_k/z)^N}{1-z_k/z}. \tag{4}$$

The rhs of Eq. (4), as the ratio of two polynomials, is by definition the Padé approximant (PA) [1]. Therefore, without any approximation, the *exact* finite-rank Green function $G_N(z^{-1})$ from (3) is reduced to the PA, which is in the field of signal processing renamed to the fast Padé transform or the FPT [1].

3.3 Various representations of the Padé response function

The fast Padé transform can have two forms, with the initial convergence region inside and outside the unit circle $|z| < 1$ and $|z| > 1$ as denoted by FPT$^{(+)}$ and FPT$^{(-)}$, respectively. The diagonal FPT corresponds to the case of equal degrees of the numerator and denominator polynomials. The most frequently used para-diagonal FPT is the one in which the degree of the numerator polynomial is by 1 smaller than that of the numerator polynomial.

The para-diagonal FPT$^{(-)}$ consists of expressing the exact finite-rank response function $G_N(z^{-1})$ by the polynomial quotient $P^-_{K-1}(z^{-1})/Q^-_K(z^{-1})$:

$$\mathrm{FPT}^{(-)} \quad : \qquad G_N(z^{-1}) \approx \frac{P^-_{K-1}(z^{-1})}{Q^-_K(z^{-1})}. \tag{5}$$

The numerator and denominator polynomials P^-_{K-1} and Q^-_K of degrees $K-1$ and K read as:

$$P^-_{K-1}(z^{-1}) = \sum_{r=0}^{K-1} p^-_r z^{-r}, \qquad Q^-_K(z^{-1}) = \sum_{s=0}^{K} q^-_s z^{-s}, \tag{6}$$

where $\{p^-_r, q^-_s\}$ are the expansion coefficients. Such coefficients are determined from the definition (5) of the FPT$^{(-)}$ via $G_N(z^{-1})Q^-_K(z^{-1}) = P^-_{K-1}(z^{-1})$. This gives a system of linear equations for $\{q^-_s\}$ and a closed, analytical expression for $\{p^-_r\}$ in terms of $\{q^-_s\}$ and $\{c_n\}$. One of several representations of the FPT$^{(-)}$ is given by the Heaviside partial fractions:

$$\frac{P^-_{K-1}(z^{-1})}{Q^-_K(z^{-1})} = \sum_{k=1}^{K} \frac{d^-_k}{z^{-1} - z^{-1}_{k,Q}}. \tag{7}$$

Quantity $z_{k,Q}^{-1}$ is the kth zero of the characteristic polynomial equation:

$$Q_K^-(z^{-1}) = 0. \tag{8}$$

This yields the nodal frequencies $\omega_{k,Q}^- = (i/\tau)\ln z_{k,Q}^{-1}$. Complex amplitudes $\{d_k^-\}$ are given by an analytical expression as the Cauchy residue of $P_{K-1}^-(z^{-1})/Q_K^-(z^{-1})$ taken at $z^{-1} = z_{k,Q}^{-1}$. In the case of non-degenerate (non-coincident) simple zeros of Eq. (8), we have:

$$d_k^- = \frac{P_{K-1}^-(z_{k,Q}^{-1})}{Q_K^{-\prime}(z_{k,Q}^{-1})}, \qquad Q_K^{-\prime}(z^{-1}) = \frac{\mathrm{d}Q_K^-(z^{-1})}{\mathrm{d}z^{-1}}, \tag{9}$$

where $Q_K^{-\prime}(z^{-1}) \neq 0$. Overall, as we see, the FPT$^{(-)}$ requires two main numerical operations to obtain the exact solution of the quantification problem. This reduces to solving a single system of linear equations for the expansion coefficients $\{q_s^-\}$ of the numerator polynomial $Q_K^-(z^{-1})$ and rooting the characteristic polynomial equation (8). An additional operation is needed to distinguish genuine from spurious resonances. This is provided by roots $\{z_{k,P}^{-1}\}$ of the characteristic equation for the numerator polynomial:

$$P_{K-1}^-(z^{-1}) = 0. \tag{10}$$

A pole-zero coincidence or confluence occurs when the solutions of Eqs. (8) and (10) are equal to each other via:

$$z_{k,Q}^{-1} = z_{k,P}^{-1}. \tag{11}$$

In this case, the associated amplitude d_k^- from (9) is automatically zero:

$$d_k^- = 0 \quad \text{for} \quad z_{k,Q}^{-1} = z_{k,P}^{-1} \quad \text{(Froissart doublet)}, \tag{12}$$

as per $P_{K-1}^-(z_{k,Q}^{-1}) = P_{K-1}^-(z_{k,P}^{-1}) = 0$. This is classified as a spurious resonance which is comprised of a pole-zero pair called a Froissart doublet [1]. The most prominent feature of spurious resonances is their marked instability against change, such as the number of signal points, the order of the polynomials, the noise level, etc. With a significant noise level, the exact pole-zero coincidence $\omega_{k,Q} = \omega_{k,P}$ may become only an approximation $\omega_{k,Q} \approx \omega_{k,P}$ for some resonances, whereas for the other resonances even such approximate confluences might disappear altogether thus yielding $\omega_{k,Q} \neq \omega_{k,P}$. Genuine resonances also have $\omega_{k,Q} \neq \omega_{k,P}$, but nevertheless they are unequivocally identified by their manifestly robust stability against the same mentioned perturbations that produce considerable alterations of parameters in spurious resonances. This possibility of differentiating between genuine and spurious resonances by their stability is unique to the fast Padé transform. Once all the spurious resonances are determined in this way, they could be discarded from the total number

of reconstructed resonances without any risk of throwing away any physical information. Such a concept is called the denoising Froissart filter (DFF). After applying the DFF, all the remaining spectral structures will be the genuine resonances with the parameters that must necessarily be identical to the true parameters of physical resonances that are present in the input data. All of these discussed characteristics will be demonstrated in the next section.

4 Results and discussion

The analysis in this section is carried out using MRS time signals given by sums of damped complex harmonics from Eq. (1). The focus of the present application is on MRS data from malignant ovarian cyst fluid. To illustrate the practical usefulness and the overall performance of the fast Padé transform, our computations will be performed with the help of the MRS time signal encoded in Ref. [40], where some twelve metabolites were estimated in the frequency interval 1–6 ppm. Therefore, for the latter frequency range, we shall set $K = 12$ in Eq. (1). The time signals from Ref. [40] were recorded using a static magnetic field strength $B_0 = 14.1\,\mathrm{T}$ (Larmor frequency ν_L of 600 MHz) and a bandwidth of 6667 Hz. The sampling time τ is the reciprocal of the bandwidth. The total signal length N was selected in Ref. [40] to satisfy the Fourier resolving power $\Delta\omega_{\min} = 2\pi/T$, where T is the total acquisition time, $T = N\tau$. This would yield a spectral resolution of $\sim$0.02 ppm, which should split apart isoleucine and valine, the two most tightly spaced metabolites, separated by 0.019 ppm. To this end, the closest integer in the composite form 2^m for the time signal length required by the FFT is $N = 2^{15} = 32768$ (32 MB).

As mentioned, the FPT resolution is not predetermined by the Fourier grid so that, in principle, a much shorter time signal length than in Ref. [40] could suffice. Therefore, we sampled our time signals using only $N = 1024$ (1 MB), which is 32 times shorter than the FID from Ref. [40]. In our computations, we used both the $\mathrm{FPT}^{(-)}$ and $\mathrm{FPT}^{(+)}$ to cross-check all the reconstructions. However, for brevity, only the results from the $\mathrm{FPT}^{(-)}$ will be reported in this work using the diagonal form $P_K^-(z^{-1})/Q_K^-(z^{-1})$ for the complex Padé spectrum. The procedure of quantification is as follows. The input data for the spectral parameters $\{\omega_k, d_k\}$ were derived from those close to the values reported in Ref. [40]. We used the quotients $2\{C_\mathrm{met}/C_\mathrm{ref}\}$ for twelve metabolites for cancerous ovarian cyst fluid obtained from twelve patients [40]. Here, $\{C_\mathrm{met}\}$ are the metabolite median concentrations expressed in μM/L ww, where ww stands for wet weight. The reference concentration C_ref was taken as the largest concentration which is 6536 μM/L ww for lactate (Lac) [40]. The phases from the complex amplitudes d_k were all set to zero, so that every amplitude d_k is, in fact, real, i.e., $d_k = |d_k|$. The line widths, that are related to $\{\mathrm{Im}(\nu_k)\}$ of the complex fundamental frequencies $\{\nu_k\}$ were estimated in Ref. [40] to be approximately 1 Hz. Here, ν_k is the linear frequency, $\nu_k = \omega_k/(2\pi)$. The chemical shifts, that are given by $\{\mathrm{Re}(\nu_k)\}$, as the positions of the nodal resonances (peaks) for the twelve metabolites are chosen to be near those from Ref. [40], but with an extended precision to three decimal places.

The input data for the present study with all the parameters and assignments for the 12 genuine metabolites are listed in Table 1. Using these parameters, the FID

Table 1 Input parameters of a simulated FID reminiscent of the in vitro MRS time signal encoded in Ref. [40] at $B_0 \approx 14.1$ T (Larmor frequency, $\nu_L = 600$ Hz) from malignant ovarian cyst fluid

INPUT DATA: SPECTRAL PARAMETERS, CONCENTRATIONS and METABOLITE ASSIGNMENTS Phases of all the input harmonics are equal to zero: $\phi_k = 0$ (k = 1, . . ., K; K = 12)					
n_k^o (Metabolite # k)	Re(ν_k) (ppm)	Im(ν_k) (ppm)	$\lvert d_k \rvert$ (au)	C_k(μM/L)	M_k (Assignment)
1	1.023	0.0008	0.024	78	Isoleucine (Iso)
2	1.042	0.0008	0.121	395	Valine (Val)
3	1.331	0.0008	0.076	248	Threonine (Thr)
4	1.412	0.0008	2.000	6536	Lactate (Lac)
5	1.513	0.0008	0.179	585	Alanine (Ala)
6	1.721	0.0008	0.150	490	Lysine (Lys)
7	2.132	0.0008	0.019	62	Methionine (Met)
8	2.473	0.0008	0.253	827	Glutamine (Gln)
9	3.052	0.0008	0.020	65	Creatine (Cr)
10	3.131	0.0008	0.024	78	Creatinine (Crn)
11	3.192	0.0008	0.013	42	Choline (Cho)
12	5.223	0.0008	0.080	261	Glucose (Glc)

Hereafter, labels Re and Im are used to denote, respectively, the real and imaginary parts of a given complex number. As such, Re(ν_k) and Im(ν_k) are the real and imaginary parts of complex fundamental frequency ν_k (both expressed in the dimensionless units, parts per million, ppm). Absolute values $|d_k|$ of amplitudes d_k are given in arbitrary units (au). Concentrations C_k of metabolites are in μM/L of wet weight (ww) of the sample. Metabolites themselves are denoted by M_k and their assignments are listed in the last column

is sampled with the help of Eq. (1) with $N = 1024$. We first employ the FPT$^{(-)}$ to solve the quantification problem for the noise-free time signal. Similarly to Ref. [11], the presently retrieved spectral parameters are found to be in exact agreement with Table 1, including all the decimals, by using barely 64 signal points, which is a very short partial signal length, $N_P = N/16 = 64$. Convergence to the known exact parameters remains fully stable for any longer partial signal lengths $N_P \leq N$. Employing the retrieved parameters, we generated the Padé-based absorption total shape spectra that are shown in Fig. 1 at two partial signal lengths, $N_P = N/16 = 64$ and $N_P = N/4 = 256$. It is seen on the right column of Fig. 1 that the spectra from the FPT remain completely unaltered despite a large difference in truncations when passing from $N_P = N/4 = 256$ (panel (iii)) to $N_P = N/16 = 64$ (panel (iv)). Specifically, the positions, heights and line widths of all the genuine resonances are identical when going from the longer ($N_P = N/4 = 256$) to a much shorter ($N_P = N/16 = 64$) fraction of the full FID, as clear from the top and bottom panels (iii) and (iv) on the right column in Fig. 1. This is in accordance with the mentioned exact reconstructions of all the spectral parameters for the twelve genuine resonances. By comparison, the FFT from the left column of Fig. 1 yields only rough, completely uninformative spectra at both signal lengths $N_P = N/16 = 64$ and $N_P = N/4 = 256$.

Next, we consider the noise-corrupted input data. To this end we add the complex-valued random zero-mean Gauss-distributed white noise of a prescribed level to the noiseless FID. The selected noise levels in this work are 10 and 25 times higher

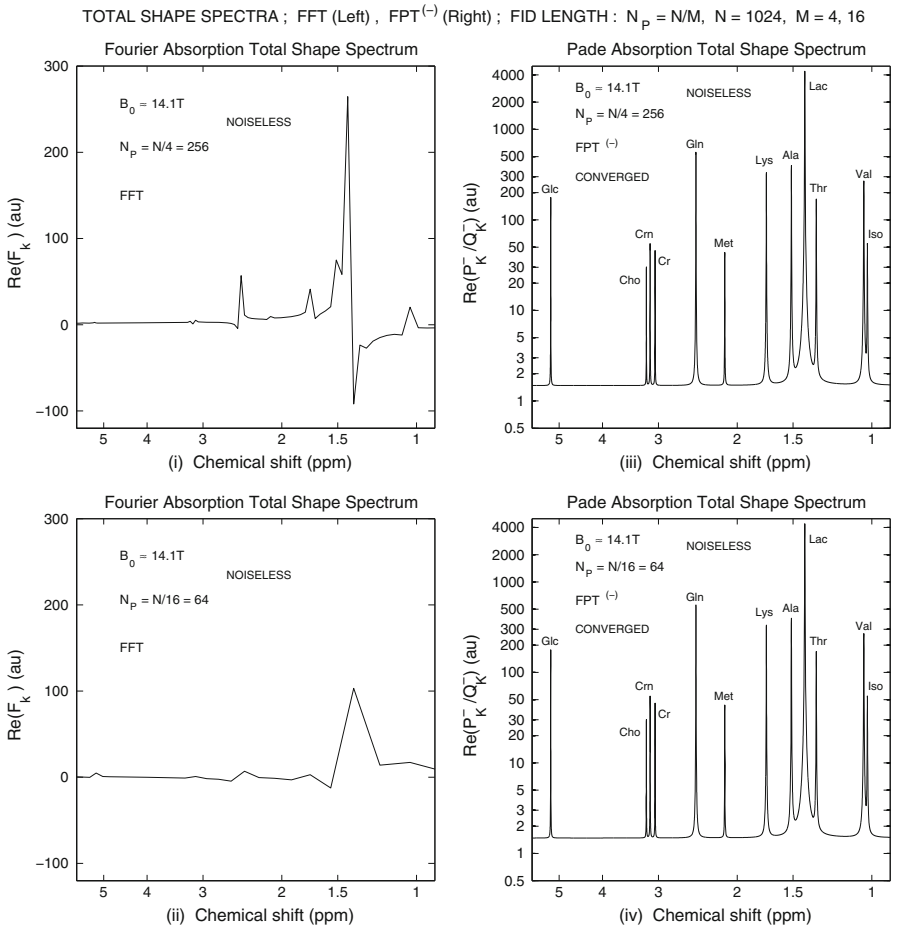

Fig. 1 Comparison of Fourier (*left column*, FFT) and Padé processing (*right column*, FPT) of a noise-free MRS time signal synthesized in accordance with the encoded FID from malignant ovarian cyst data of Ref. [40]. Hereafter, abscissa represents chemical shifts, as dimensionless linear frequencies ν, given in parts per million (ppm), ordinates are the real parts of complex-valued spectra in arbitrary units (au) and ν_{L} is the Larmor frequency. Convergence of the total absorption shape spectrum in the fast Padé transform, FPT, on the right column is attained with $N_{\mathrm{P}} = N/16 = 64$ signal points (*panel* (*iv*)) and remains stable for longer signal lengths, as illustrated in *panel* (*iii*) at $N_{\mathrm{P}} = 256$. The fast Fourier transform, FFT, on the left column yields only rough and totally uninformative spectra at these same partial signal lengths N_{P}. The Fourier spectra at $N_{\mathrm{P}} = 256$ (*panel* (*i*)) and $N_{\mathrm{P}} = N/16 = 64$ (*panel* (*ii*)) differ markedly from each other, with the prominent peak at frequency 1.5 ppm broadened and attenuated in the latter. Convergence with Fourier processing requires 32768 signal points (32 MB). This is some formidable 512 and 128 times longer input data set compared to the time signal length used in Padé processing from *panels* (*iv*) and (*iii*), respectively

than that in Ref. [11] in which the standard deviation of noise was $\sigma = 0.01156$ RMS, where RMS is the root-mean-square of the noise-free time signal (RMS $=$ 1.6472). The reconstructed parameters for the noise-corrupted time signal with $\sigma =$ 0.1156 RMS are shown in Tables 2, 3, 4 and 5, for 3 partial signal lengths $N_{\mathrm{P}} =$ $256(N/4), 512(N/2), 910$ as well as for the full FID ($N = 1024$). Three of them

Table 2 Padé-based reconstruction of spectral parameters and concentrations of metabolites using a noise-corrupted simulated FID reminiscent of the in vitro MRS time signal encoded in Ref. [40] at $B_0 \approx 14.1$ T (Larmor frequency, $\nu_L = 600$ Hz) from malignant ovarian cyst fluid

RECONSTRUCTION of SPECTRAL PARAMETERS and CONCENTRATIONS in FPT$^{(-)}$:
NOISY INPUT DATA
Noise: $\sigma = 0.1156$ RMS; signal length: $N_P = N/4 = 256$, N = 1024

n_k^o (Metabolite # k)	Re(ν_k^-) (ppm)	Im(ν_k^-) (ppm)	$\lvert d_k^- \rvert$ (au)	C_k^- (μM/L)	M_k^- (assignment)
–	−0.073	0.0433	0.001	3	Spurious
–	0.688	0.0341	0.001	3	Spurious
1	1.023	0.0009	0.025	82	Isoleucine (Iso)
2	1.042	0.0008	0.120	392	Valine (Val)
–	1.167	0.0708	0.001	3	Spurious
3	1.331	0.0008	0.076	248	Threonine (Thr)
4	1.412	0.0008	2.000	6536	Lactate (Lac)
5	1.513	0.0008	0.179	585	Alanine (Ala)
6	1.721	0.0008	0.150	490	Lysine (Lys)
–	1.813	0.0257	0.001	3	Spurious
–	1.840	0.3681	0.031	101	Spurious
–	2.131	0.2656	0.029	95	Spurious
7	2.132	0.0008	0.019	62	Methionine (Met)
–	2.339	0.1655	0.011	36	Spurious
8	2.473	0.0008	0.253	827	Glutamine (Gln)
9	3.052	0.0008	0.020	65	Creatine (Cr)
10	3.131	0.0008	0.024	78	Creatinine (Crn)
11	3.192	0.0009	0.014	46	Choline (Cho)
–	3.396	0.0257	0.001	3	Spurious
–	4.242	0.2061	0.006	20	Spurious
–	4.543	0.0398	0.003	10	Spurious
–	4.572	0.0536	0.005	16	Spurious
12	5.223	0.0008	0.080	261	Glucose (Glc)

Added to the noiseless time signal, built from the input parameters given in Table 1, is the complex-valued zero-mean random Gaussian-distributed noise of level $\sigma = 0.1156$ RMS, where RMS is root-mean-square of the noise-free FID. Partial signal length employed is $N_P = N/4 = 256$, where N is the total length of the FID ($N = 1024$)

($N_P = 256, 512, 1024$) satisfy the FFT-required relation $N_P = 2^m$ or $N_P = N/M$ where $M = 4, 2, 1$ and $m = 8, 9, 10$ (Tables 2, 3, 5). Such a type of truncation is only optional in the FPT where any positive integer can be used for the partial signal length N_P as shown in Table 4 where $N_P = 910$. The degree K_T of the diagonal fast Padé transform P_{K_T}/Q_{K_T} is equal to $N_P/2$ for any fixed partial FID length thus yielding some $N_P/2$ reconstructed metabolites. These include the $K = K_G$ genuine constituents of the FID from Eq. (1) where $K = 12$. The difference $K_T - K_G$ represents the number of the spurious resonances since they are absent from the noiseless input data given in Table 1. As emphasized, the main identifying signature of spurious

Table 3 Padé-based reconstruction of spectral parameters and concentrations of metabolites using a noise-corrupted simulated FID reminiscent of the in vitro MRS time signal encoded in Ref. [40] at $B_0 \approx 14.1$ T (Larmor frequency, $\nu_L = 600$ Hz) from malignant ovarian cyst fluid

RECONSTRUCTION of SPECTRAL PARAMETERS and CONCENTRATIONS in FPT$^{(-)}$: NOISY INPUT DATA
Noise: $\sigma = 0.1156$ RMS; signal length: $N_P = N/2 = 512$, $N = 1024$

n_k^o (Metabolite # k)	Re(ν_k^-) (ppm)	Im(ν_k^-) (ppm)	$\lvert d_k^- \rvert$ (au)	C_k^- (μM/L)	M_k^- (assignment)
–	−0.861	0.0307	0.002	7	Spurious
–	−0.668	0.1007	0.006	20	Spurious
–	−0.546	0.0426	0.003	10	Spurious
–	−0.366	0.1202	0.005	16	Spurious
–	0.289	0.0337	0.002	7	Spurious
–	0.423	0.0427	0.002	7	Spurious
–	0.478	0.0308	0.002	7	Spurious
–	0.827	0.0642	0.006	20	Spurious
–	0.884	0.0198	0.003	10	Spurious
–	0.916	0.0245	0.003	10	Spurious
1	1.023	0.0008	0.024	78	Isoleucine (Iso)
2	1.042	0.0008	0.121	395	Valine (Val)
3	1.331	0.0008	0.076	248	Threonine (Thr)
4	1.412	0.0008	2.000	6536	Lactate (Lac)
5	1.513	0.0008	0.179	585	Alanine (Ala)
6	1.721	0.0008	0.150	490	Lysine (Lys)
–	1.733	0.0484	0.004	13	Spurious
–	1.761	0.2202	0.025	82	Spurious
–	2.049	0.0639	0.004	13	Spurious
7	2.132	0.0008	0.019	62	Methionine (Met)
–	2.183	0.1674	0.034	111	Spurious
–	2.275	0.0781	0.006	20	Spurious
–	2.422	0.2764	0.035	114	Spurious
8	2.473	0.0008	0.253	827	Glutamine (Gln)
9	3.052	0.0008	0.020	65	Creatine (Cr)
10	3.131	0.0008	0.024	78	Creatinine (Crn)
11	3.192	0.0009	0.013	42	Choline (Cho)
–	3.379	0.0699	0.005	16	Spurious
–	3.597	0.0437	0.002	7	Spurious
–	3.988	0.6300	0.022	72	Spurious
–	5.058	0.0378	0.002	7	Spurious
–	5.146	0.0190	0.001	3	Spurious
12	5.223	0.0008	0.080	261	Glucose (Glc)

Added to the noiseless time signal, built from the input parameters given in Table 1, is the complex-valued zero-mean random Gaussian-distributed noise of level $\sigma = 0.1156$ RMS, where RMS is root-mean-square of the noise-free FID. Partial signal length employed is $N_P = N/2 = 512$, where N is the total length of the FID ($N = 1024$)

Table 4 Padé-based reconstruction of spectral parameters and concentrations of metabolites using a noise-corrupted simulated FID reminiscent of the in vitro MRS time signal encoded in Ref. [40] at $B_0 \approx 14.1$ T (Larmor frequency, $\nu_L = 600$ Hz) from malignant ovarian cyst fluid

RECONSTRUCTION of SPECTRAL PARAMETERS and CONCENTRATIONS in FPT$^{(-)}$: NOISY INPUT DATA
Noise: $\sigma = 0.1156$ RMS; signal length: $N_P = 910$, $N = 1024$

n_k^o (Metabolite # k)	Re(ν_k^-) (ppm)	Im(ν_k^-) (ppm)	$\lvert d_k^- \rvert$ (au)	C_k^- (μM/L)	M_k^- (assignment)
–	−0.554	0.0513	0.003	10	Spurious
–	−0.024	0.0499	0.002	7	Spurious
–	−0.002	1.3796	0.004	13	Spurious
–	0.376	0.0604	0.001	3	Spurious
–	0.639	0.0473	0.003	10	Spurious
1	1.023	0.0008	0.024	78	Isoleucine (Iso)
2	1.042	0.0008	0.121	395	Valine (Val)
3	1.331	0.0008	0.076	248	Threonine (Thr)
4	1.412	0.0008	2.000	6536	Lactate (Lac)
5	1.513	0.0008	0.179	585	Alanine (Ala)
–	1.678	0.0292	0.001	3	Spurious
–	1.713	0.0076	0.001	3	Spurious
6	1.721	0.0008	0.150	490	Lysine (Lys)
7	2.132	0.0008	0.019	62	Methionine (Met)
–	2.445	0.6287	0.007	23	Spurious
8	2.473	0.0008	0.253	827	Glutamine (Gln)
–	2.977	0.0122	0.001	3	Spurious
–	3.005	0.0124	0.001	3	Spurious
–	3.025	0.2106	0.013	42	Spurious
9	3.052	0.0008	0.020	65	Creatine (Cr)
–	3.056	0.0194	0.002	7	Spurious
10	3.131	0.0008	0.024	78	Creatinine (Crn)
11	3.192	0.0008	0.013	42	Choline (Cho)
–	3.196	0.0210	0.001	3	Spurious
–	3.491	0.0271	0.002	7	Spurious
–	4.160	0.0387	0.004	13	Spurious
–	4.169	0.0223	0.002	7	Spurious
–	4.325	0.0167	0.001	3	Spurious
–	4.365	0.0571	0.005	16	Spurious
–	4.782	0.0136	0.002	7	Spurious
–	5.187	0.0644	0.005	16	Spurious
12	5.223	0.0008	0.080	261	Glucose (Glc)

Added to the noiseless time signal, built from the input parameters given in Table 1, is the complex-valued zero-mean random Gaussian-distributed noise of level $\sigma = 0.1156$ RMS, where RMS refers to the root-mean-square of the noise-free FID. The number of signal points employed is $N_P = 910$ out of $N = 1024$, which is total length of the FID

Table 5 Padé-based reconstruction of spectral parameters and concentrations of metabolites using a noise-corrupted simulated FID reminiscent of the in vitro MRS time signal encoded in Ref. [40] at $B_0 \approx 14.1$ T (Larmor frequency, $\nu_L = 600$ Hz) from malignant ovarian cyst fluid

RECONSTRUCTION of SPECTRAL PARAMETERS and CONCENTRATIONS in FPT$^{(-)}$: NOISY INPUT DATA
Noise: $\sigma = 0.1156$ RMS; signal length: $N_P = N = 1024$

n_k^o (Metabolite # k)	Re(ν_k^-) (ppm)	Im(ν_k^-) (ppm)	$\lvert d_k^- \rvert$ (au)	C_k^- (μM/L)	M_k^- (assignment)
–	−0.659	0.0108	0.001	3	Spurious
–	−0.574	0.1078	0.006	20	Spurious
–	−0.439	0.4570	0.020	65	Spurious
–	−0.100	0.0610	0.005	16	Spurious
–	0.338	0.0589	0.002	7	Spurious
–	0.516	0.0566	0.004	13	Spurious
–	0.579	0.0115	0.001	3	Spurious
–	0.608	0.0222	0.004	13	Spurious
–	0.608	0.0075	0.001	3	Spurious
1	1.023	0.0008	0.024	78	Isoleucine (Iso)
2	1.042	0.0008	0.121	395	Valine (Val)
–	1.236	0.0631	0.002	7	Spurious
3	1.331	0.0008	0.076	248	Threonine (Thr)
–	1.392	0.0130	0.001	3	Spurious
–	1.404	0.0475	0.004	13	Spurious
4	1.412	0.0008	2.000	6536	Lactate (Lac)
5	1.513	0.0008	0.179	585	Alanine (Ala)
–	1.713	0.0075	0.002	7	Spurious
6	1.721	0.0008	0.150	490	Lysine (Lys)
–	1.730	0.0306	0.003	10	Spurious
–	1.948	0.1151	0.005	16	Spurious
7	2.132	0.0008	0.019	62	Methionine (Met)
–	2.173	0.0385	0.002	7	Spurious
8	2.473	0.0008	0.253	827	Glutamine (Gln)
–	2.737	0.0206	0.001	3	Spurious
–	2.917	0.0401	0.002	7	Spurious
–	2.972	0.0152	0.001	3	Spurious
9	3.052	0.0008	0.020	65	Creatine (Cr)
10	3.131	0.0008	0.024	78	Creatinine (Crn)
11	3.192	0.0008	0.013	42	Choline (Cho)
–	3.873	0.1292	0.003	10	Spurious
–	4.064	0.0256	0.001	3	Spurious
–	4.846	0.0423	0.002	7	Spurious
–	4.866	0.0108	0.001	3	Spurious

Table 5 continued

RECONSTRUCTION of SPECTRAL PARAMETERS and CONCENTRATIONS in FPT$^{(-)}$: NOISY INPUT DATA
Noise: $\sigma = 0.1156$ RMS; signal length: $N_P = N = 1024$

n_k^o (Metabolite # k)	Re(ν_k^-) (ppm)	Im(ν_k^-) (ppm)	$\lvert d_k^- \rvert$ (au)	C_k^- (μM/L)	M_k^- (assignment)
–	4.965	0.1664	0.011	36	Spurious
–	5.206	0.1528	0.010	33	Spurious
12	5.223	0.0008	0.080	261	Glucose (Glc)

Added to the noiseless time signal, built from the input parameters given in Table 1, is the complex-valued zero-mean random Gaussian-distributed noise of level $\sigma = 0.1156$ RMS, where RMS is root-mean-square of the noise-free FID. The full signal length $N = 1024$ is employed

resonances is their pronounced instability manifested by changing e.g. N_P, noise level, etc. This is evident from Tables 2, 3, 4 and 5 for 4 signal lengths ($N_P = 256, 512, 910, 1024$).

Among all the reconstructions, some 116, 244, 443, 500 spurious resonances are found at $N_P = 256, 512, 910, 1024$, respectively. To avoid displaying such large numbers of data in Tables 2, 3, 4 and 5, only small fractions are given for these parameters of spurious resonances with a cut-off value $|d_k| \geq 0.001$ for the absolute value of the found amplitudes. As seen in Table 1, this is by about an order of magnitude smaller than the associated lowest value of $|d_k|$ among genuine resonances, corresponding to choline having $|d_k| = 0.013$. With the threshold of $|d_k| \geq 0.001$ for retaining all the retrieved resonances, Tables 2, 3, 4, 5 show that there are still some 11, 21, 20, 25 remaining spurious peaks at $N_P = 256, 512, 910, 1024$, respectively. Just like all the other found unphysical data from the whole Nyquist range $(-1, 10)$ ppm, the spurious resonances reported in Tables 2, 3, 4 and 5 markedly alter their parameters when changing the partial signal length according to $N_P = 256, 512, 910, 1024$, respectively.

The proof-of-principle of the concept of the denoising Froissart filter, or the DFF, is given in Figs. 2, 3, 4, 5 and 6. Figure 2 compares the FPT-based reconstructions using the noiseless and noisy ($\sigma = 0.01156$ RMS) input data as in Ref. [11]. Therein, panels (i) and (ii) show the Argand plots for noise-corrupted and noise-free input data, respectively. Panel (iii) of the same Fig. 2 displays the reconstructed absolute values of the amplitudes for the noisy FID. At all the three panels (i)–(iii), also depicted are the exact noiseless input parameters. It can be seen that despite the presence of noise, the FPT is able to reconstruct exactly the noiseless input parameters. This amounts to noise reduction by the fast Padé transform. Both spectral poles and zeros are shown on panels (i) and (ii). Froissart doublets are clearly seen by the exact pole-zero coincidences in these two panels. Denser noiseless spurious resonances appear to be quite regularly aligned in a chain on panel (ii). This is not the case with the corresponding denser noisy spurious resonances that are misaligned as they are perturbed by noise of level $\sigma = 0.01156$ RMS. Precise pole-zero confluences yield exactly zero-valued amplitudes and this is evidenced on panel (iii) of Fig. 2. Therein, the auxiliary horizontal line at the zero value of the ordinate crosses exactly through the centers of open circles for all the spurious amplitudes. The absolute values of the

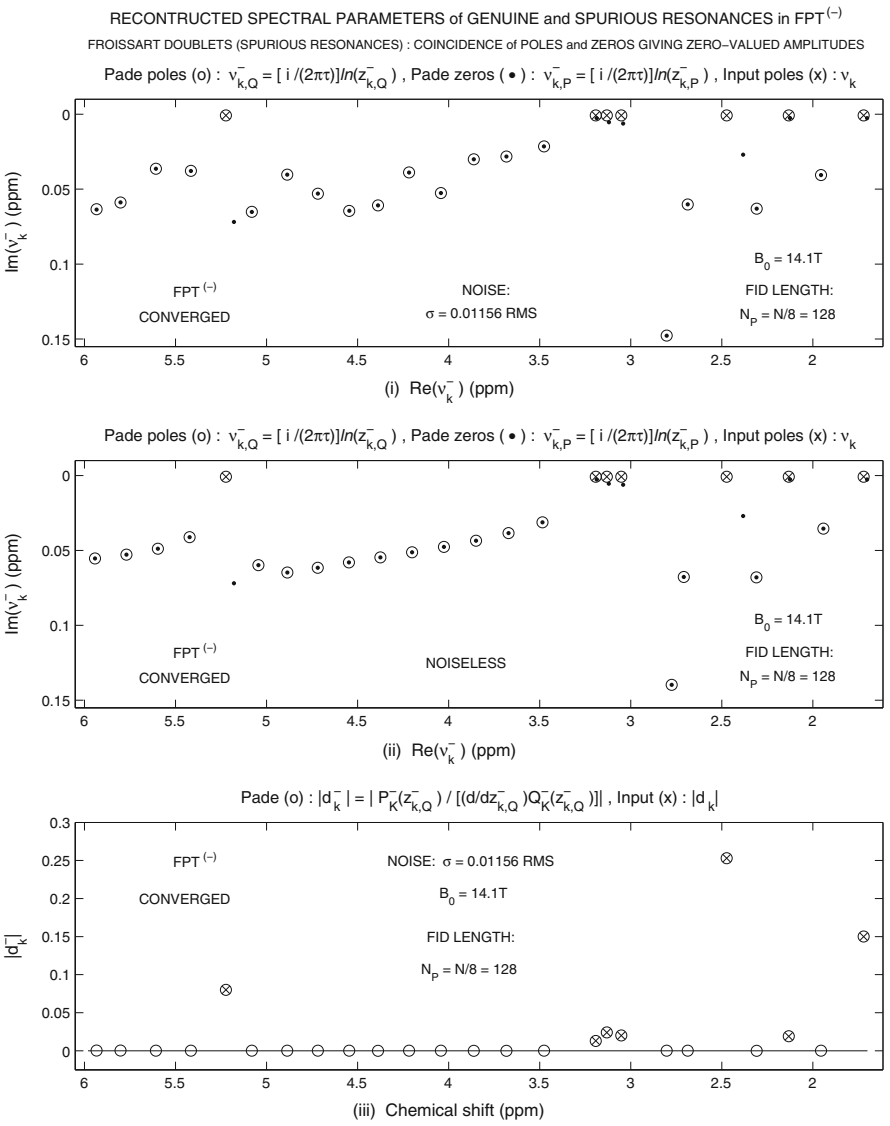

Fig. 2 Separation of genuine from spurious resonances for noise-free and noise-corrupted FID of the same partial signal length. Padé-based reconstruction of spectral frequencies and absolute values of amplitudes using a simulated FID reminiscent of the in vitro MRS time signal encoded in Ref. [40] at $B_0 \approx 14.1$ T (Larmor frequency, $\nu_L = 600$ Hz) from malignant ovarian cyst fluid. Partial signal length employed is $N_P = N/8 = 128$, where N is the total length of the FID ($N = 1024$). *Panel (ii)* is for noise-free time signal, whereas *panel* (*i*) is for noise-corrupted FID. To the noiseless time signal synthesized with the input parameters from Table 1 added is the complex-valued zero-mean random Gaussian-distributed noise of level $\sigma = 0.01156$ RMS, where RMS is root-mean-square of the noise-free FID

reconstructed amplitudes from panel (iii) are explicitly drawn for noisy input data, but the same results are obtained by using the noiseless time signal.

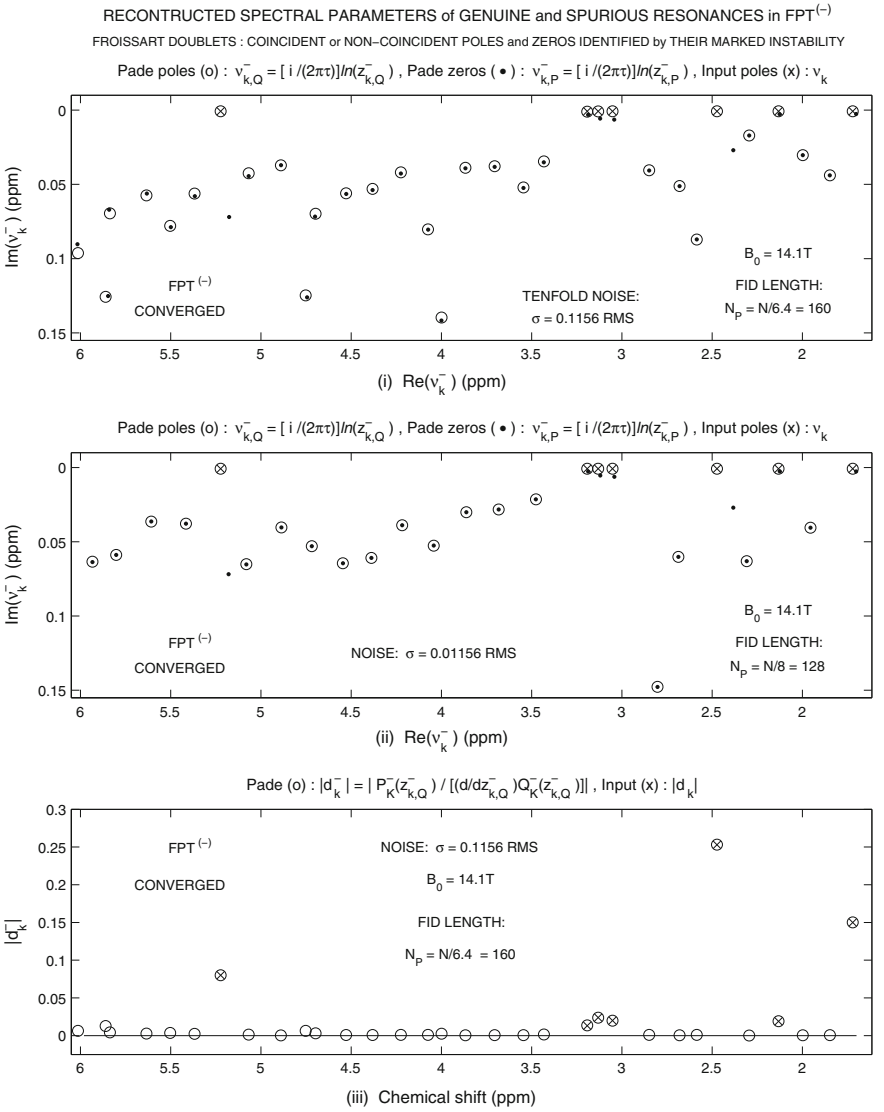

Fig. 3 Separation of genuine from spurious resonances. Padé-based reconstruction of spectral frequencies and absolute values of amplitudes using a simulated noisy FID reminiscent of the in vitro MRS time signal encoded in Ref. [40] at $B_0 \approx 14.1$ T (Larmor frequency, $\nu_L = 600$ Hz) from malignant ovarian cyst fluid. Partial signal lengths employed are $N_P = N/8 = 128$ and $N_P = N/6.4 = 160$ where N is the total length of the FID ($N = 1024$). To the noiseless time signal synthesized with the input parameters from Table 1 added is the complex-valued zero-mean random Gaussian-distributed noise of levels $\sigma = 0.1156$ RMS and $\sigma = 0.01156$ RMS on *panels* (*i*) and (*ii*), respectively, where RMS is root-mean-square of the noise-free FID

Figure 3 compares the reconstructions by the FPT employing two non-zero noise levels that differ by a factor of ten, $\sigma = 0.01156$ RMS and $\sigma = 0.1156$ RMS. We used two different partial signal lengths, one satisfying the Fourier-prescribed form

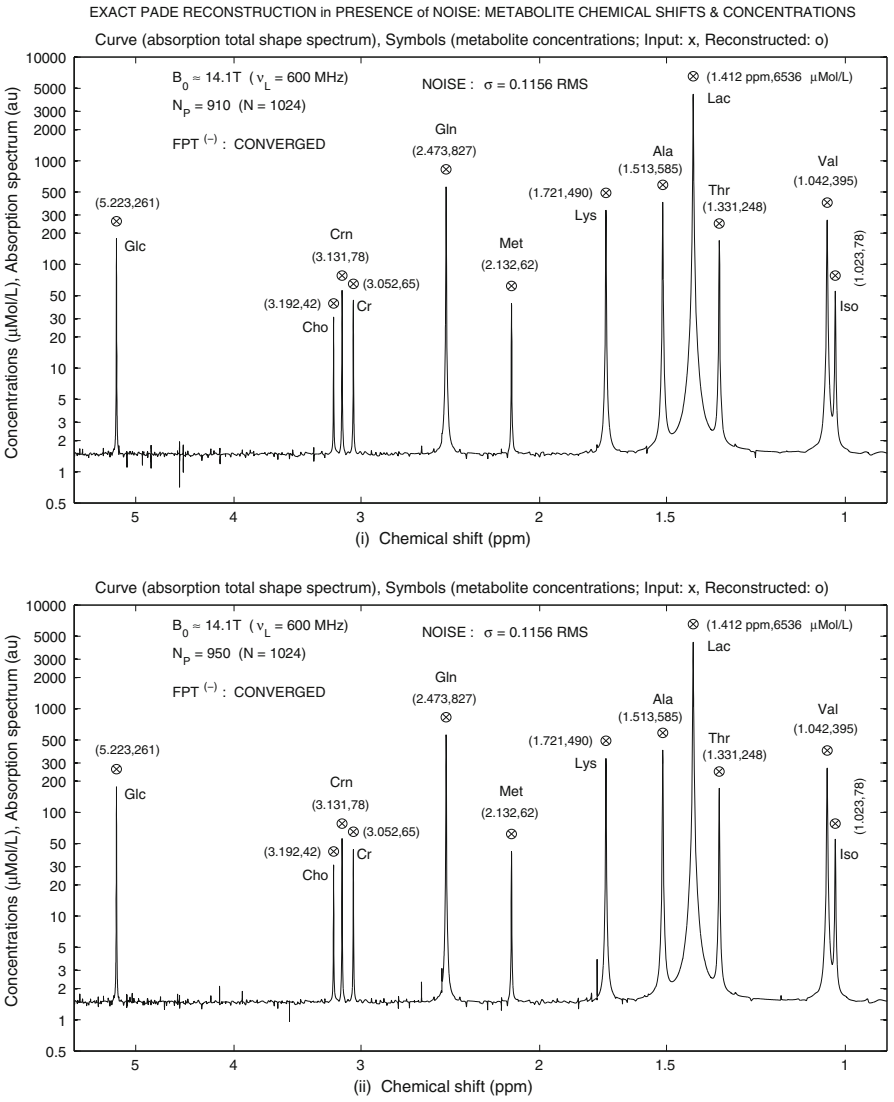

Fig. 4 Envelope stability test for the same noise level and two different partial signal lengths. Padé-based reconstruction of spectral envelopes as well as of chemical shifts and concentrations of metabolites using a simulated noisy FID reminiscent of the in vitro MRS time signal encoded in Ref. [40] at $B_0 \approx 14.1$ T (Larmor frequency, $\nu_L = 600$ Hz) from malignant ovarian cyst fluid. The numbers of signal points employed are $N_P = 910$ and $N_P = 950$ out of $N = 1024$, which is total length of the FID. To the noiseless time signal synthesized with the input parameters from Table 1 added is the complex-valued zero-mean random Gaussian-distributed noise of level $\sigma = 0.1156$ RMS, where RMS is root-mean-square of the noise-free FID

2^m with $m = 5$ i.e. $N_P = N/8 = 128$ and the other $N_P = 160$ which corresponds to a truncation by a factor of 6.4 ($N_P = 160 = N/6.4$). For both noise levels, the fast Padé transform reconstructs exactly all the noiseless input parameters. Spurious

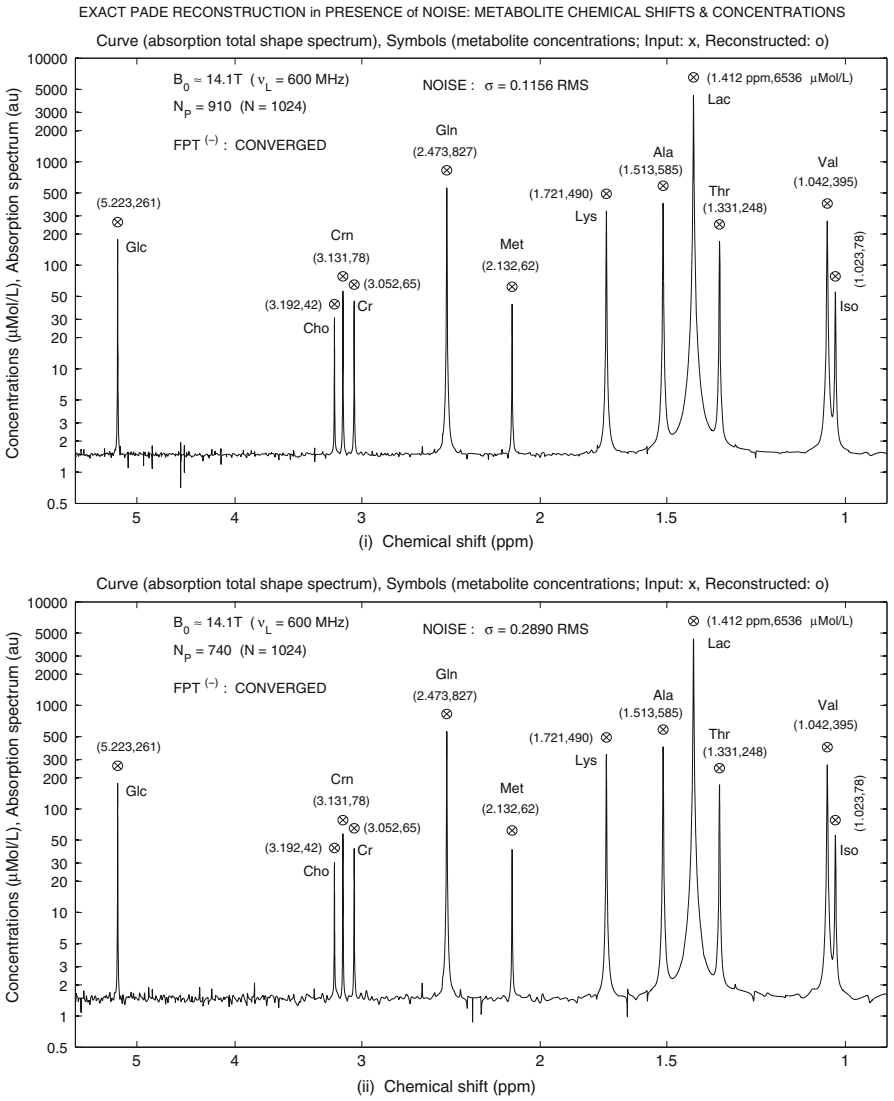

Fig. 5 Envelope stability test for two different noise levels and two different partial signal lengths. Padé-based reconstruction of spectral envelopes as well as of chemical shifts and concentrations of metabolites using a simulated noisy FID reminiscent of the in vitro MRS time signal encoded in Ref. [40] at $B_0 \approx 14.1$ T (Larmor frequency, $\nu_L = 600$ Hz) from malignant ovarian cyst fluid. The numbers of signal points employed are $N_P = 740$ and $N_P = 910$ out of $N = 1024$, which is total length of the FID. To the noiseless time signal synthesized with the input parameters from Table 1 added is the complex-valued zero-mean random Gaussian-distributed noise of levels $\sigma = 0.1156$ RMS and $\sigma = 0.2890$ RMS on *panels* (*i*) and (*ii*), respectively, where RMS is root-mean-square of the noise-free FID

resonances in the Argand plots look more chaotic on panel (i) for $\sigma = 0.1156$ RMS than on panel (ii) for $\sigma = 0.01156$ RMS. Moreover, with the tenfold increase of the noise level on panel (i), some of spurious resonances do not exhibit exact pole-zero

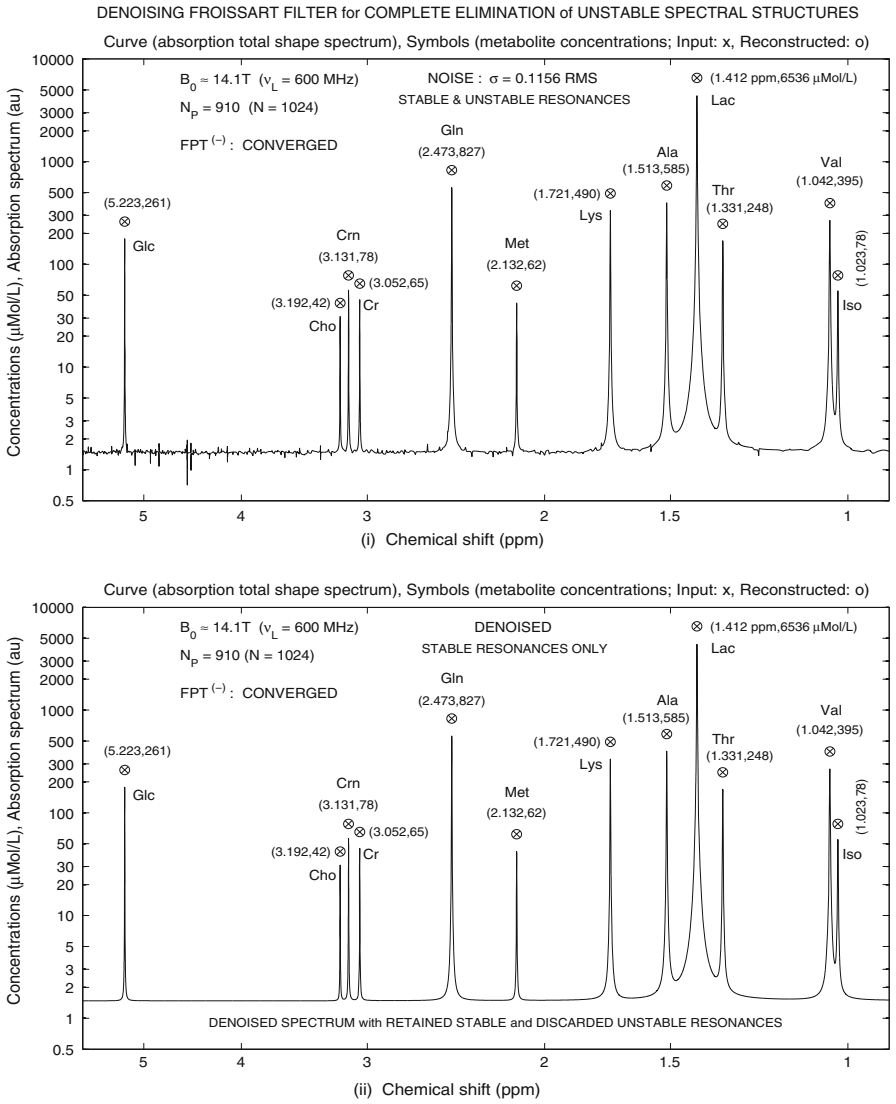

Fig. 6 Denoising (noise elimination) from noise-corrupted envelope. Padé-based reconstruction of spectral envelopes as well as of chemical shifts and concentrations of metabolites using a simulated noisy FID reminiscent of the in vitro MRS time signal encoded in Ref. [40] at $B_0 \approx 14.1$ T (Larmor frequency, $\nu_{\mathrm{L}} = 600\,\mathrm{Hz}$) from malignant ovarian cyst fluid. The number of signal points employed is $N_{\mathrm{P}} = 910$ out of $N = 1024$, which is the total length of the FID. To the noiseless time signal synthesized with the input parameters from Table 1 added is the complex-valued zero-mean random Gaussian-distributed noise of level $\sigma = 0.1156$ RMS on *panel* (*i*), where RMS is root-mean-square of the noise-free FID. *Panel* (*ii*) shows the denoised spectrum obtained by binning the noisy output data through retaining stable and discarding unstable resonances via the denoising Froissart filter

confluence or such a coincidence does not occur at all. This is also confirmed on panel (iii) where some of the spurious amplitudes are not zero, as clearly shown by the auxiliary horizontal line on the zero height. In particular, it is seen that one of the

spurious resonances near 5.8 ppm has nearly the same height as genuine resonance at 3.192 ppm (Cho) and the question arises as to how these two can be distinguished. Such questions are vital when dealing with encoded time signals for which the true peak parameters are unknown and an objective criterion must be used to disentangle the physical and unphysical information.

In Figs. 4, 5 and 6 we illustrate the stability test which answers these questions. Thus, Fig. 4 shows the absorption total shape spectra at the same noise level ($\sigma = 0.1156$ RMS), but at two different partial signal lengths ($N_P = 910, 950$). It is seen in Fig. 4 that at this noise level the reconstructed chemical shifts and concentrations of all the 12 genuine resonances are identical to the corresponding noiseless input data. This implies stability of the retrieved physical resonances. Such a stability is robust since it persists despite the tenfold increase of noise relative to $\sigma = 0.01156$ RMS from Ref. [11]. In contradistinction, by a relatively mild increase in the partial signal length from $N_P = 910$ to $N_P = 950$, all the remaining spectral structures are seen to fluctuate on the background level due to the induced changes in the underlying parameters (peak positions, widths, heights, phases). Due to this noticeable instability, the latter spectral structures are unphysical, extraneous, i.e. spurious.

Figure 5 shows an alternative stability test where both the partial signal length and the noise level are simultaneously varied. On panel (i) of this figure, we use $N_P = 910$ and $\sigma = 0.1156$, whereas panel (ii) corresponds to $N_P = 740$ and $\sigma = 0.2890$ with the latter noise level being 2.5 times in excess of the former. Despite this significant increase in the noise level, as also evident on the background in panel (ii), the fast Padé transforms is still seen to be capable of exact retrieval of all the 12 noiseless chemical shifts and concentrations for genuine metabolites. The remaining spectral structures on panel (ii) are completely different from the corresponding background on panel (i) in every aspect and this instability identifies them as spurious resonances in agreement with the conclusion from Fig. 4 as well as from Ref. [13].

The performed error analysis based on the test of stability of all the reconstructed parameters as well as constancy of the resulting spectral shapes in the whole Nyquist range (a part of which was illustrated in the tables and figures) enables an unequivocal separation of the true from the false information in the analyzed data. This constitutes the concept of signal-noise separation or SNS. With the disentangled genuine from spurious resonances, the output data can be binned into the physical and unphysical groups or sectors. Thus, by retaining the physical group and discarding the unphysical sector of the reconstructed data, exact reconstruction of the noiseless input data becomes, in principle, possible despite considerable perturbation by complex random zero-mean Gaussian noise of the standard deviation $\sigma = 0.01156, 0.1156, 0.2890$ RMS which was the subject of the effected checks. In other words, if this binning of the output list is explicitly carried out, it would be expected that we are finally left only with the true, noiseless input parameters and the corresponding denoised absorption spectrum. Indeed, this is the case, as exemplified in Fig. 6 for the noise-corrupted FID with standard deviation $\sigma = 0.1156$. Panel (i) of Fig. 6 shows the output noisy spectrum constructed by using all the 455 found resonances ($K_{tot} = 455 = N_P/2$, $N_P = 910$) in the whole Nyquist interval $(-1, 10)$ ppm. Exclusion of the 443 unstable resonances as spurious yields the 12 stable resonances, that are the genuine content of the input data, effectively amounts to denoising the noisy

spectrum from panel (i). The ensuing denoised spectrum is shown on panel (ii) in Fig. 6 and is seen as indistinguishable from the associated noiseless spectrum of the FPT from Fig. 1.

4.1 Clinical implications of these most recent findings for ovarian cancer

In the presence of some 10–25 higher noise levels than in Ref. [11], the FPT provided excellent resolution and exact reconstruction of all physical metabolite concentrations characteristic of malignant ovarian cyst fluid. In vivo MRS has been envisioned as the potential method of choice for early stage ovarian cancer detection. However, this would require overcoming the barriers obstructing the acquisition of high quality time signals and subsequent trustworthy analysis of spectra. Molecular imaging through MRS could, therefore, have much broader applications in screening surveillance for early ovarian cancer detection, particularly among women at high risk. This possibility is attractive because there is no exposure to ionizing radiation. These results strongly suggest that Padé-optimization will be a critical step towards improving the diagnostic accuracy of MRS for ovarian cancer. Better outcomes are thereby anticipated for women afflicted with this malignancy.

4.2 Broader significance for oncology

Magnetic resonance spectroscopy is a crucial modality for oncology [16–23,33,34, 36,41,42]. It is, therefore, essential to overcome the problems hindering more widespread application of MRS in cancer diagnostics and care of patients with cancer. As explained, more advanced signal processing methods are vital to these efforts and the fast Padé transform, FPT, is the signal processing method of choice [1–15].

Application of the FPT to in vivo MRS signals encoded from the brain on high field (3, 4, 7 T) and clinical (1.5 T) scanners shows that over 20 metabolite concentrations can be reliably determined. This is to be compared to at most 5 metabolite concentrations retrieved by the "FFT alongside fitting" approaches [2,3,13]. Such findings are expected to have major implications for brain tumor diagnostics, and post-therapeutic patient care [14,26]. In particular, the improved image-guided target definition provided by Padé-optimized MRS will be essential in combination with better input to dose-planning systems for RT, as provided by our recently introduced Padé linear-quadratic (PLQ) model for cell response to radiation damage [43–45]. The link between these two areas has been suggested in Ref. [45], where it was noted that cell survival probabilities could be used to assess changes in metabolite concentrations post-RT as a method for delineating the target volume for patients who undergo re-irradiation.

The potential advantages of Padé-optimization are also clearly demonstrated for MRS data from prostate, breast and ovarian cancer. Previously, in each of these areas, the diagnostic yield of MRS had been severely limited by reliance upon the "FFT together with fitting" approaches. Our results [4,7,13,14] illustrate that the FPT can resolve and exactly quantify a large number of overlapping resonances, including multiplets of metabolites that distinguish normal glandular prostate, normal stromal

prostate and prostate cancer. Thus, MRS with the accompanying Padé quantification applied to prostate cancer is particularly important for diagnostic enhancement, because of the current dilemmas surrounding prostate cancer screening (e.g. cut-points of prostate specific antigen, PSA), clinical decision-making for high- versus low-risk prostate cancer, identifying sites for biopsy, as well as for targeting dominant intraprostatic lesions, where an escalated radiation dose might be delivered with better sparing of the surrounding normal tissue [14,42]. Here again, this is expected to be particularly advantageous in conjunction with better input to dose-planning systems for RT, as provided by the PLQ model [43–45].

The results from Refs. [4,8,9,13] for MRS data from the cancerous breast, fibroadenoma and normal breast, showed the advantages of the Padé-optimization, especially for areas of high spectral density. The FPT resolves and exactly quantifies extremely closely-lying resonances, including phosphocholine, a marker of malignant transformation of the breast. This line of investigation is being continued by ourselves with in vivo data from benign and malignant breast tissue. We anticipate that Padé-optimized MRS will reduce the false positive rates of MR-based modalities and further improve their sensitivity. Once this is achieved, and since MR entails no ionizing radiation, new possibilities for screening/early detection will open up, especially for risk groups. For example, Padé-optimized MRS could be used with greater surveillance frequency among younger women at high breast cancer risk. Surveillance after breast cancer treatment could also be more frequent, as well as more effective with Padé-optimized MRS.

The FPT applied to benign and malignant ovarian fluid, dramatically improved resolution compared to FFT-based processing and provided highly accurate determination of key metabolite concentrations for identifying ovarian cancer. The present results indicate that via Padé-processing, excellent resolution with exact determination of metabolite concentrations can be achieved for ovarian cancer MRS time signals in the presence of noise. These features of the FPT are anticipated to be of critical benefit to ovarian cancer diagnostics by MRS, particularly for early detection, a goal which has been elusive, and achievement of which would confer a major survival advantage.

An important next step is to perform comparative analysis between clinical (1.5 T) scanners and higher-field MR scanners. This has a significant practical side, including economic, since 1.5 T scanners are the most abundant in hospitals worldwide, due to their price which is much lower than for stronger magnets. For far too long, experience originating in analytical chemistry has been exported to medical diagnostics through MR via focusing mainly on hardware improvements by increasing magnetic field strength with the aim of improving resolution. This strategy has not met with palpable success in MRS, because the corresponding advances in signal processing were precluded by virtually exclusive reliance upon the conventional data analytic methods with the FFT and fitting.

Instead, we are pursuing a less frequently traveled road by maximally exploring the alternative avenue of gaining resolution improvement in MRS with ordinary 1.5 T scanners by means of better equipped mathematics in optimization of signal processing. This is a "quantum leap" which is in the realm of new wider horizons, as it sets the researcher's mind on the promising pathway of mathematical modeling using, e.g.,

our methodology of the fast Padé transform which could be widely implemented at the most abundant MR scanners (1.5 T).

Thus far, MRS has made great strides by relying upon a mere handful of metabolites, or even a single metabolite, e.g., total choline for breast cancer. This severely restricted metabolite window stems directly from the limitations of the FFT combined with fitting and other related phenomenological approaches with adjustable parameters. It is expected that the diagnostic yield of MRS in oncology will be significantly enhanced by extracting reliable information about many more metabolites. This is directly facilitated by the FPT, on the basis of its proven validity, theoretically supported by quantum physics and algorithmically confirmed in robust computations. This basic science input is needed. Starting as the well-established nuclear magnetic resonance (NMR) spectroscopy in physics and analytical chemistry, MRS has developed to such a point in medicine that it is currently being viewed by experts as the modality which has the potential to revolutionize not only diagnostics, but also molecular-image-guided surgery and target delineation for radiotherapy [16,17,19–23,41,42].

4.3 How will this strategy help MRS become part of standard diagnostics in clinical oncology?

This strategy is multifaceted encompassing acquisition, analysis and clinical interpretation of the MRS data encoded from patients with cancer. The middle part (data analysis) of this chain amounts to finding the unequivocal solution of the quantification problem through decomposition of the encoded data into its true metabolic constituents. This is accomplished by the FPT. Remarkably, we see from the inner workings of the FPT that its role is not limited to data analysis alone. On the contrary, the very manner by which the FPT achieves high resolution dictates a complete reformulation of the concept of data acquisition, by encoding a small number of short time signals to secure good SNR. The FPT is also directly implicated in clinical interpretation by enlarging the diagnostic window through detecting at least 20 true metabolites, in sharp contrast to merely 5 from conventional FFT-based data analysis.

4.3.1 Impossibility of a forced trade off within FFT: accuracy versus long examination time

A major problem of MRS has been low SNR. This was partially mitigated by averaging about 200 time signals requiring long scan times for the patient. All the conventional methods in MRS exclusively rely upon the FFT for this full averaged time signal. This requires long acquisition time to overcome low SNR. Since MRS time signals decay exponentially over time, at larger times mainly noise is measured. Hence the need to have shorter time signals to secure better SNR, since earlier encoded signal intensities are well above the background noise level. Because of this fundamental theoretical limitation of the FFT, it is impossible to shorten the examination time of patients and still achieve accuracy with good SNR.

4.3.2 Direct clinical benefits of overcoming the FFT conundrum by the FPT

The FPT eliminates the need for the said trade-off by providing accuracy plus good SNR while simultaneously shortening the total examination time, thus making MRS more efficient. This is possible because the frequency resolution in the FPT spectrum is not constrained at all by the total signal length N. Consequently, time signals of short length suffice for the FPT, which exploits the ensuing good SNR to obtain the required frequency resolution in spectra. Figure 1 testifies to this achievement. Varying the partial signal length N_P for the same fixed bandwidth is equivalent to varying the acquisition times. In the FFT, to achieve the required clinical accuracy by e.g. resolving the two most closely-lying resonances (isoleucine and valine), one needs an extremely long time signal obtained by averaged some 200 times signals each of huge length of $N = 32768$ (32 MB). By contrast, the FPT splits apart isoleucine and valine with a time signal of only 256 data points. This latter signal length is a remarkable 128 times shorter than $N = 32768$ needed in the FFT. Such a huge amount of truncation results in dramatically improved SNR and, therefore, in increased accuracy through high resolution.

4.3.3 Impact of the FPT on the data acquisition system in MRS: clinical relevance

In general, the FFT and FPT envelope spectra could be similar, but only for very low amount of truncation of the total time signal length. For higher amounts of truncation, FFT spectra are severely distorted and exhibit broadened peaks. This results in low resolution, poor accuracy with major information loss, as clearly seen in Fig. 1. Simultaneously, peaks from the FPT spectra remain sharp and well resolved with their true widths unaltered even for extremely high levels of truncation. Here lies a distinct practical advantage in using the FPT for large amounts of truncation of the time signal data to significantly shorten overall acquisition times in MRS. Encoding shorter time signals automatically yields higher SNR and this, in turn, necessitates a smaller number of time signals of the order of at most 30. A further improvement of SNR is obtained by averaging these 30 encoded time signals. The subsequent quantification of the averaged time signals of low SNR by the FPT gives the sought optimal accuracy with a much shorter acquisition time. However, there is an alternative to this "signal averaging" which we call "parameter averaging". In this alternative, we process independently all the 30 encoded time signals and reconstruct 30 sets of the spectral parameters for all the true resonances. The final set of reconstructions is obtained by averaging all the 30 sets of values of each parameters. This automatically gives the standard deviation of the reconstructed parameters in the same spirit as the error bars that are conventionally obtained in virtually all measurements.

4.3.4 Padé-guided MRS with distinct clinical advantages

The outlined strategy is of direct clinical relevance foremost because of the long sought better diagnostic accuracy of MRS with a bonus of shorter examination times. This improves the turn-around time for patients, making MRS an efficient and

cost-effective diagnostic modality. Thus, better equipped mathematics via the FPT provide not only exact quantification of MRS data, but can also fundamentally change the way MRS time signals are encoded. Overall, the FPT has a significant advantage in SNR over the FFT. This is because the FPT needs only short time signals compared to conventional acquisitions using the FFT. For short time signals, the FFT yields uninterpretable spectra, as seen is Fig. 1. As such, the new encoding of short time signals will presuppose the use of the FPT. It is in this way that the FPT directly influences the measurements by designing the manner in which time signals should be encoded to enhance the overall performance of MRS.

5 Conclusion

We have provided the proof-of-principle for exact reconstructions of all the genuine parameters for physical metabolites from MRS time signals in the presence of noise of the levels that are 10–25 times higher than in the previous study using the fast Padé transform, the FPT. This was made possible by reliance upon the concept of signal-noise separation, or SNS, consisting of unequivocal identification of genuine or physical and spurious or unphysical resonances. The SNS is accomplished by performing the stability tests of the reconstructed parameters and the generated spectral shapes. It was shown that at the varying partial signal length and noise level, some of the retrieved resonances fluctuate, whereas the others do not. Fluctuations signify alterations of positions, heights, widths and phases of resonant peaks for different noise levels and for varying truncations of the total signal length. This implies that such resonances of peaks are unstable and, therefore, cannot represent the true constituent of the physical spectrum. In sharp contrast, the other resonances that do not change with variations of partial signal lengths and noise levels are manifestly stable and, as such, are identified as the genuine content of the true spectrum. All these features are presently exemplified through applications to the FIDs that are reminiscent to the vitro MRS time signals encoded from the ovarian malignant tissue. The fast Fourier transform or FFT for the analyzed FIDs in the noiseless case necessitates the signal length of 32 MB to resolve all the physical resonances. By comparison, all the listed achievements are made by the FPT using a short signal of only length 0.5 MB. This conclusion is of a great practical usefulness, since it obviates the need for the Fourier-imposed request of repeated acquisition of long time signals, the procedure which entails a long turn-around time for patients' scanning. Therefore, with the Padé-based quantification alongside the FPT-guided encoding of MRS data of considerably reduced length, MRS can become a reliable, cost-effective tool for diagnostics and various aspects of patient care within clinical oncology.

Acknowledgments This work was supported by the Swedish Cancer Society (Cancerfonden) Fund, Radiumhemmet Research Fund through the Karolinska University Hospital, the Karolinska Institute Research Fund and the Stockholm City Council (FoUU) Fund to which the authors are grateful.

References

1. Dž. Belkić, *Quantum Mechanical Signal Processing and Spectral Analysis* (Institute of Physics Publishing, Bristol, 2005)
2. Dž. Belkić, Exact quantification of time signals in Padé-based magnetic resonance spectroscopy. Phys. Med. Biol. **51**, 2633 (2006)
3. Dž. Belkić, Exponential convergence rate of the FPT for exact quantification in MRS. Phys. Med. Biol. **51**, 6483 (2006)
4. Dž. Belkić, K. Belkić, *Signal Processing in MRS with Biomedical Applications* (Taylor & Francis, London, 2010)
5. Dž. Belkić, Parametric analysis of time signals and spectra from perspectives of quantum physics. Adv. Quantum Chem. **61**, 145 (2011)
6. Dž. Belkić, K. Belkić, High-resolution signal processing in MRS for early cancer diagnostics. Adv. Quantum Chem. **62**, 245 (2011)
7. Dž. Belkić, K. Belkić, Unequivocal resolution of multiplets in MRS for prostate cancer by the FPT. J. Math. Chem. **45**, 819 (2009)
8. Dž. Belkić, K. Belkić, Exact quantification of time signals from MRS by the FPT applied to breast cancer. J. Math. Chem. **45**, 790 (2009)
9. K. Belkić, Dž. Belkić, Possibilities for improved early breast cancer detection by Padé-optimized MRS. Isr. Med. Assoc. J. **13**, 236 (2011)
10. Dž. Belkić, K. Belkić, Mathematical modeling applied to an NMR problem in ovarian cancer detection. J. Math. Chem. **43**, 395 (2008)
11. Dž. Belkić, K. Belkić, MRS with high-resolution and exact quantification in the presence of noise: ovarian cancer. J. Math. Chem. **50**, 2558 (2012)
12. Dž. Belkić, K. Belkić, The fast Padé transform in MRS for improvements in early cancer diagnostics. Phys. Med. Biol. **50**, 4385 (2005)
13. Dž. Belkić, K. Belkić, Practical improvements in cancer diagnostics by mathematically-optimized MRS. J. Math. Chem. **49**, 2408 (2011)
14. Dž. Belkić, K. Belkić, Molecular imaging and magnetic resonance for improved target definition in radiation oncology, in *Radiation Damage to Biomolecular Systems*, ed. by G. Gómez, M.C. Fuss (Springer, Berlin, 2012), pp. 411–429
15. Dž. Belkić, Exact signal-noise separation by Froissart doublets in the fast Padé transform for magnetic resonance spectroscopy. Adv. Quantum Chem. **56**, 95 (2009)
16. J. Evelhoch, M. Garwood, D. Vigneron, M. Knopp, D. Sullivan, A. Menkens A, L. Clarke, G. Liu, Expanding the use of magnetic resonance in the assessment of tumor response to therapy. Cancer Res. **65**, 7041 (2005)
17. C. Marcus, Imaging techniques to evaluate response to treatment in oncology. Crit. Rev. Oncol.-Hemat. **72**, 217 (2009)
18. W. Hollingworth, L.S. Medina, R.E. Lenkinski, D.K. Shibata, B. Bernal, D. Zurakowski, B. Comstock, J.G. Jarvik, A systematic literature review of MRS for the characterization of brain tumors. Am. J. Neuroradiol. **27**, 1404 (2006)
19. H. Hričak, MR imaging and MR spectroscopic imaging in the pre-treatment evaluation of prostate cancer. Br. J. Radiol. **78**, S103 (2005)
20. L. Kwock, J. Smith, M. Castillo, M. Ewend, F. Collichio, D. Morris, T. Bouldin, S. Cush, Proton magnetic resonance spectroscopy in oncology: brain, breast and prostate cancer. Lancet Oncol. **7**, 859 (2006)
21. L. Bell, N.L. Ainsworth, S.H. Lee, J.R. Griffiths, MRI and MRS assessment of the role of tumor micro-environment in response to therapy. NMR Biomed. **24**, 612 (2011)
22. K. Glunde, J. Jiang, S.A. Moestue, I.S. Gribbestad, MRS/MRSI guidance in molecular medicine: targeting choline and glucose metabolism. NMR Biomed. **24**, 673 (2011)
23. R. Kauppinen, A.C. Peet, MRI and MRS in cancer diagnostics and monitoring. Cancer Biol. Ther. **12**, 665 (2011)
24. K. Belkić, Dž. Belkić, Spectroscopic imaging through magnetic resonance for brain tumor diagnostics. J. Comp. Meth. Sci. Engin. **4**, 157 (2004)
25. N. Morita, M. Harada, H. Otsuka, E.R. Melhem, H. Nishitani, Clinical application of MR spectroscopy and imaging of brain tumor. Magn. Reson. Med. Sci. **9**, 167 (2010)

26. Dž. Belkić, K. Belkić, Meta-analysis of studies using magnetic resonance spectroscopy to assess suspicious lesions post-RT of primary brain tumors. J. Math. Chem. **50**, 2527 (2012)
27. V. Kumar, N.R. Jagannathan, S. Thulkar, R. Kumar, Pre-biopsy MRS and imaging in the diagnosis of prostate cancer. Int. J. Urol. **19**, 602 (2012)
28. K. Belkić, *Molecular Imaging Through Magnetic Resonance for Clinical Oncology* (Cambridge International Science Publishing, Cambridge, 2004)
29. A. Shukla-Dave, H. Hričak, P.T. Scardino, Imaging low-risk prostate cancer. Curr. Opin. Urol. **18**, 78 (2008)
30. V. Kundra, P.M. Silverman, S.F. Matin, H. Choi, Imaging in oncology: diagnosis, staging and surveillance of prostate cancer. Am. J. Roentgenol. **189**, 830 (2007)
31. M. Swanson, A. Zektzer, Z. Tabatabai, J. Simko, S. Jarso, K. Keshari, L. Schmitt, P. Carroll, K. Shinohara, D. Vigneron, J. Kurhanewicz, Quantitative analysis of prostate metabolites using 1H HR-MAS spectroscopy. Magn. Reson. Med. **55**, 1257 (2006)
32. D. Saslow, C. Boetes, W. Burke, S. Harms, M.O. Leach, C.D. Lehman, E. Morris, E. Pisano, M. Schnall, S. Sener, R.A. Smith, E. Warner, M. Yaffe, K.S. Andrews, C.A. Russell, American Cancer Society Breast Cancer Advisory Group. American Cancer Society guidelines for breast screening with MRI as an adjunct. CA Cancer J. Clin. **57**, 75 (2007)
33. G. Tse, D. Yeung, A. King, H. Cheung, W. Yang, In vivo MRS of breast lesions: an update. Breast Cancer Res. Treat. **104**, 249 (2007)
34. J.K. Begley, T.W. Redpath, F.J. Gilbert, *In vivo* proton MRS of breast cancer: a review of the literature. Breast Cancer Res. **14**, 207 (2012)
35. L. Gluch, Magnetic resonance in surgical oncology. ANZ J. Surg. **75**, 464 (2005)
36. R. Katz-Brull, P.T. Lavin, R.E. Lenkinski, Clinical utility of MRS in characterizing breast lesions. J. Natl. Cancer Inst. **9**, 1197 (2002)
37. Dž. Belkić, K. Belkić, Mathematical optimization in NMR through the FPT for breast cancer detection. J. Math. Chem. **40**, 85 (2006)
38. I. Gribbestad, B. Sitter, S. Lundgren, J. Krane, D. Axelson, Metabolite composition in breast tumors examined by NMR. Anticancer Res. **19**, 1737 (1999)
39. A. Esseridou, G. Di Leo, L.M. Sconfienza, V. Caldiera, F. Raspagliesi, B. Grijuela, F. Hanozet, F. Podo, F. Sardanelli, *In vivo* detection of choline in ovarian tumors using 3D MRS. Investig. Radiol. **46**, 377 (2011)
40. E. Boss, S.H. Moolenaar, L.F.A.G. Massuger, H. Boonstra, U.F.H. Engelke, J.G.N. de Jong, R.A. Wevers, High-resolution proton nuclear magnetic resonance spectroscopy of ovarian cyst fluid. NMR Biomed. **13**, 297 (2000)
41. C.E. Mountford, S. Doran, C.L. Lean, P.L. Russell, Proton MRS can determine the pathology of human cancers with high accuracy. Chem. Rev. **104**, 3677 (2004)
42. T. Joseph, D.A. McKenna, A.C. Westphalen, F.V. Coakley, S. Zhao, Y. Lu, I.C. Hsu, M. Roach, J. Kurhanewicz, MRI/MRSI in prostate cancer as predictors of response to external beam radiotherapy. Int. J. Radiat. Oncol. Bio. Phys. **73**, 665 (2009)
43. Dž. Belkić, K. Belkić, Mechanistic repair-based Padé linear-quadratic model for cell response to radiation damage. Adv. Quantum Chem. **65**, 407 (2013)
44. B. Andisheh, M. Edgren, Dž. Belkić, P. Mavroidis, A. Brahme, B. Lind, A comparative analysis of radio-biological models for cell surviving fractions at high doses. Technol. Cancer Res. Treat. **12**, 183 (2013)
45. Dž. Belkić, K. Belkić, Padé–Froissart exact signal-noise separation in nuclear magnetic resonance spectroscopy. J. Phys. B: Atom. Mol. Opt. Phys. **44**, 125003 (2011)